Alternating magneto-birefringence of ionic ferrofluids in crossed fields

E. Hasmonay[1], E. Dubois[2], S. Neveu[2], J.-C. Bacri[1,a], and R. Perzynski[1,b]

[1] Laboratoire des Milieux Désordonnés et Hétérogènes, Université Pierre et Marie Curie (Paris 6), Tour 13, Case 78, 4 place Jussieu, 75252 Paris Cedex 05, France

[2] Laboratoire des Liquides Ioniques et Interfaces Chargées, Université Pierre et Marie Curie (Paris 6), bâtiment F, Case 63, 4 place Jussieu, 75252 Paris Cedex 05, France

Abstract. A dynamic probing of magnetic liquids is performed experimentally, using a static magnetic field modulated by another smaller field, normal and alternating. The optical magneto-birefringence under these crossed magnetic fields is recorded as a function of the frequency for different field intensities and different sizes of the magnetic nanoparticles. A general reduced behavior is found for the in-phase and the out-of-phase optical response which is well-described by a simple mechanical model. Depending on the value H_{ani} of the anisotropy field of the nanoparticles, we can distinguish two different high magnetic field regimes: – a rigid dipole regime (large anisotropy energy with respect to $k_{\mathrm{B}}T$) for cobalt ferrite nanoparticles with a relaxation time inversely proportional to the field intensity $H_{\mathrm{C}}(H_{\mathrm{C}} < H_{\mathrm{ani}})$, – a soft dipole regime (anisotropy energy of the order of $k_{\mathrm{B}}T$) for maghemite nanoparticles with a relaxation time independent of the field intensity $H_{\mathrm{C}}(H_{\mathrm{C}} > H_{\mathrm{ani}})$.

PACS. 75.50.Mm Magnetic liquids – 78.20.Ls Magnetooptical effects – 78.67.Bf Optical properties of nanocrystals and nanoparticles

1 Introduction

Magnetic fluids [1] (or ferrofluids) are colloidal suspensions of nanosized particles. The carrier can be either a simple liquid either a more complex medium such as a gel or a lyotropic solution [2–4]. The magneto-optical properties of the particles in response to a pulse of magnetic field can be used to determine some dynamic quantities such as the viscosity of the external medium if it is a liquid [5,6], the hydrodynamic radius of the particles [7] or the elastic constant of the carrier [2,8,9]. These particles being nanoscopic probes of the carrier medium, it should be possible to determine its viscoelastic properties as a function of frequency, with a measure of the magneto-optical answer to an alternating external magnetic field. Having in mind this long range prospect, we propose here an original experimental set-up able to determine these viscoelastic constants from 1 Hz to 10 kHz: we measure the dynamic magnetic birefringence of the colloidal system submitted to two crossed magnetic fields one large and static $\mathbf{H}_{\mathrm{C}}$, the second being alternating and small. To validate this method, we explore here the dynamic answer of maghemite and cobalt ferrites particles, 10 nm-sized, suspended in a simple liquid carrier: glycerol. We

show that the optical dynamics depend on the nanoparticle anisotropy. Several regimes are sorted out theoretically and evidenced experimentally. They correspond to different hierarchies between the applied static field and the internal anisotropy field of the particles.

2 Mechanical model

The principle of the experimental method is the following. Monodomain and optically uniaxial, magnetic nanoparticles are dispersed in a liquid and submitted to two crossed magnetic fields. One, $\mathbf{H}_{\mathrm{C}}$, is large and static, the second $\mathbf{H}_{\mathrm{A}}$ is alternating and much smaller. The large static field $\mathbf{H}_{\mathrm{C}}$ orientates on average the magnetic moments of the particles together with their optical axis along $\mathbf{H}_{\mathrm{C}}$. The magnetic moment of the nanoparticles may achieve thermal equilibrium along the field through two different processes: Brownian rotation or Néel relaxation, leading respectively to extrinsinc or intrinsic superparamagnetism [10,11].

– For Brownian rotation, moment alignments are achieved by a mechanical rotation of the whole particle in the carrier liquid, magnetic moment being locked in an easy direction of magnetization.

– Néel relaxation is a rotation of the magnetic moment away from the easy direction within the particle. An
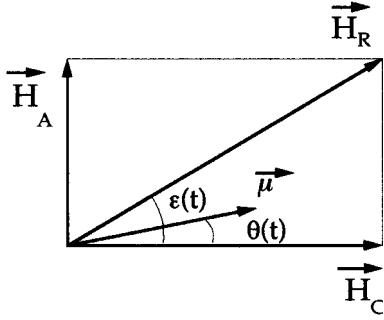
Fig. 1. Orientation of the magnetic fields of the experiment together with that of the magnetic moment $\boldsymbol{\mu}$ of a nanoparticle; The angles θ and ε are defined in the text.

energy barrier, namely the anisotropy energy E_a, hinders this rotation. A characteristic time of the Néel process is $\tau_N = \tau_0 \exp(E_a/kT)$ with $\tau_0 \approx 10^{-9}$ s.

In a liquid solution both mechanisms occur. The dominant process of orientation of the magnetic moment is determined by the shortest characteristic time [12,13]. For its part, the birefringence of the solution is closely related to a mechanical alignment of the particle body along the field. Ferrofluid particles prevented from moving by being quenched in a tight gel network do not exhibit birefringence but still exhibit magnetization. Here the alternating field $\mathbf{H}_A$ modulates the direction of the magnetic moments at its own frequency, the body of the particle being coupled to the magnetic moment through the anisotropy. In the experiment we detect the mechanical response to this sollicitation. We develop below a simple mechanical model to describe the movement of a single magnetic particle in the solvent. This description is valid in the limit of low volume fractions of magnetic particles, where the interparticle interactions can be neglected.

2.1 Rigid dipole ($E_a \gg kT$)

Assuming first that the magnetic moment of the particle is rigidly tied to its optical axis, we neglect for a time the intrinsic superparamagnetism for the particle. In this approximation, the anisotropy energy E_a of the particle is much greater than the thermal energy $k_B T$. The applied field $\mathbf{H}_R$ resulting from the superposing of the static field $\mathbf{H}_C$ crossed with the alternating field $\mathbf{H}_A$ writes $\mathbf{H}_R = \mathbf{H}_C + \mathbf{H}_A$ with $H_A/H_C \ll 1$. Its amplitude is:

$$H_R \approx H_C \left(1 + \frac{H_A^2}{2H_C^2} \cos^2(\omega t) \right). \tag{1}$$

The angle $\varepsilon(t) = (\mathbf{H}_C, \mathbf{H}_R)$ (see Fig. 1) is time-dependent and is directly connected to the orientation of $\mathbf{H}_R$. At low frequency and in the framework of the rigid dipole approximation, the time dependence of the angle $\theta(t)$ (see Fig. 1) between the magnetic moment $\boldsymbol{\mu}$ and $\mathbf{H}_A$ is equal to $\varepsilon(t)$. Neglecting the thermal energy, $\theta(t)$ is given by:

$$J\frac{d^2\theta}{dt^2} + 6\eta V_h \frac{d\theta}{dt} + \mu_0\mu H_C \sin\theta = \mu_0\mu H_A \cos\theta \cos\omega t, \tag{2}$$

where η is the solvent viscosity, V_h the hydrodynamic volume of the particle, and where J is its moment of inertia. Inertia can be always neglected here. J being of the order of 10^{-38} J s^2, the first term is several orders of magnitude smaller than all the other terms of equation (2). In the limit $\theta \ll 1$, equation (2) reduces to:

$$6\eta V_h \frac{d\theta}{dt} + \mu_0\mu H_C \theta = \mu_0\mu H_A \cos\omega t. \tag{3}$$

Using complex notations, it comes $\varepsilon(t) \approx (H_A/H_C)e^{i\omega t}$ and:

$$\theta(t) = \tilde{\theta}e^{i\omega t} \quad \text{with} \quad \tilde{\theta} = \theta_0 \frac{1}{1 + i\omega\tau} \tag{4}$$

with $\theta_0 = H_A/H_C$ and τ the characteristic relaxation time of the magnetic particle (equivalent to a Debye relaxation time for a dielectric medium). The value τ_H of τ is here given by:

$$\tau_H = \frac{6\eta V_h}{\mu_0\mu H_C}. \tag{5}$$

Let us note that, as the magnetic moment μ is proportional to the volume of the particle, τ_H is at the first order, independent of the particle size.

If now the thermal agitation is taken into account as in reference [14], the expression of the characteristic time τ becomes:

$$\tau_\perp = \frac{2\tau_B L_1(\xi_C)}{\xi_C - L_1(\xi_C)} \tag{6}$$

where τ_B is the Brownian rotation diffusion time defined as

$$\tau_B = \frac{3\eta V_h}{k_B T}, \tag{7}$$

$L_1(\xi) = \coth(\xi) - 1/\xi$ is the Langevin function, and $\xi_C = \mu_0\mu H_C/k_B T$ is the value of the Langevin parameter for the static field H_C. Figure 2 presents the field dependence of $\tau_\perp$.

In the limit of weak magnetic fields $\xi_C \ll 1$, the static field H_C has not a sufficient amplitude to struggle against the thermal broadening. The characteristic time $\tau_\perp$ then reduces to the Brownian rotational time and $\tau_\perp \approx \tau_B$.

As H_C increases, the characteristic relaxation time decreases progressively. In the high fields limit $\xi_C \gg 1$, one meets again the expression (5): $\tau_\perp \approx 2\tau_B/\xi_C = \tau_H$. The direction of the magnetic moment of the nanoparticle is modulated around the direction of the static magnetic field. The large anisotropy energy rigidly ties the magnetic moment to the crystalline body of the particle. The magnetic energy being much larger than the thermal energy $k_B T$, the relaxation now occurs with the characteristic time τ_H.

In summary, in the limit $\xi_C \ll 1$, the particles relax towards random directions under the influence of thermal agitation. In the limit $\xi_C \gg 1$ they relax towards the magnetic field direction. For large magnetic field ($\xi_C \gg 1$) and infinitely large anisotropy energy ($E_a \gg \mu_0\mu H_C \gg k_B T$),
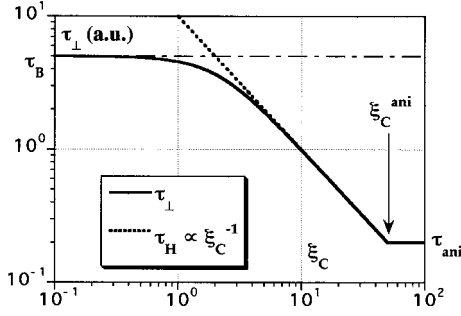
Fig. 2. Theoretical representation of the characteristic time $\tau_\perp$ (in arbitrary units) as a function of the Langevin parameter ξ_C for $\sigma = 25$. At $\xi_C = 0$ $\tau_\perp = \tau_B$ (Eq. (7)). For $1 \ll \xi_C < \xi_C^{\text{ani}}$ (standard rigid dipole regime) $\tau_\perp = \tau_H \propto \xi_C^{-1}$ (Eq. (5)). At the first order, τ_H is particle size independent. ξ_C^{ani} is the value of ξ_C for the anisotropy field H_{ani}. For $\xi_C > \xi_C^{\text{ani}}$ $\tau_\perp = \tau_{\text{ani}}$ (Eq. (8)).

$\tau_\perp$ decays as: $\tau_\perp \propto \xi_C^{-1}$. It would mean $\tau_\perp \to 0$ as $\xi_C \to \infty$. In Figure 2, the dotted line marks for rigid dipoles the field behavior $\tau_\perp = \tau_H$. At the first order it is particle size independent. On the contrary, the low field behavior $\tau_\perp = \tau_B$ is strongly size dependent. Experimentally the high field regime will be reached at a higher field for smaller particles.

2.2 Influence of the anisotropy field

If the uniaxial magnetic anisotropy energy E_a of the nanoparticles is no more infinite with respect to thermal energy, the movement of the particle body does not reduce anymore just to the movement of their magnetic moments. We distinguish here the soft dipole limit ($\sigma = E_a/k_B T \approx 1$) from the superparamagnetic limit ($\sigma \ll 1$). For $\sigma \ll 1$, the fluctuations of the magnetic moment are completely decorrelated from those of the magnetic body of the nanoparticle and thus do not induce any birefringence.

For $\sigma \approx 1$, a new parameter has to be considered in our description [15], the anisotropy field H_{ani}. It is linked to the magnetic anisotropy energy by $E_a = \frac{1}{2}\mu_0 \mu H_{\text{ani}}$ and modifies the problem which can be modeled as follows. Under the applied magnetic field, the magnetic moment first orientates along the direction of the applied field. Then in a second step, an internal elastic restoring force, due to the particle anisotropy field H_{ani}, makes the particle body to rotate in order to replace the magnetic moment along the easy axis direction. If the external magnetic field H_C is large with respect to the anisotropy field ($H_C \gg H_{\text{ani}}$), the internal elastic restoring force dominates [15]. The relaxation occurs with a characteristic time $\tau = \tau_{\text{ani}}$ such as:

$$\tau_{\text{ani}} = 6\eta V_h/\mu_0 \mu H_{\text{ani}} = \tau_B/\sigma \qquad (8)$$

(see Fig. 3). Thanks to this process the high field limit of the relaxation characteristic time is no more equal to zero but equal to τ_{ani}. For magnetic fields H_C much smaller than H_{ani}, the hypotheses of the rigid dipole model can
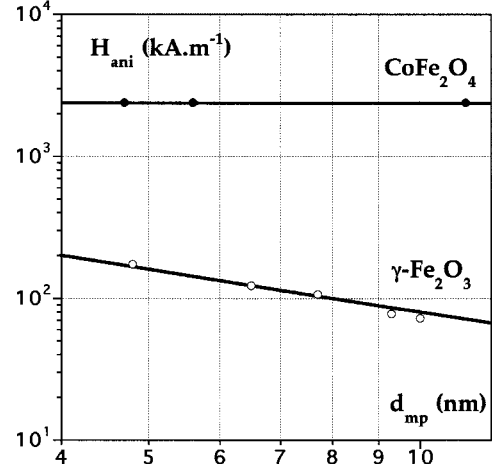
Fig. 3. Anisotropy field H_{ani} for cobalt ferrite and maghemite magnetic nanoparticles as a function of the most probable diameter d_{mp}. The experimental values come from references [22–24]. Full lines have respectively a slope zero for $CoFe_2O_4$ and a slope -1 for γ-Fe_2O_3.

be restored with $\tau = \tau_\perp$ in a window of magnetic fields ($1 \ll \xi_C < \xi_C^{\text{ani}}$) if σ is large enough.

3 Experiments

3.1 Ferrofluids

3.1.1 Synthesis

The ferrofluids used in the experiments are ionic ferrofluids chemically synthesized after Massart's method [16,17]. The nanoparticles of our samples are made of an iron oxide: either maghemite (γ-Fe_2O_3) or cobalt ferrite ($CoFe_2O_4$). The magnetic liquids are obtained by alkalization of aqueous solutions of Fe[II] and Fe[III] salts [17,18] for the maghemite samples, and by coprecipitation in an alkaline medium of aqueous solutions of Fe[III] chloride and Co[II] nitrate for the cobalt ferrite samples [19]. The synthesized particles are then coated with a superficial density of charged citrate ligands. The electrostatic interparticle repulsion allows their stable dispersion in glycerin ($C_3H_8O_3$). It is a Newtonian viscous fluid. Viscosity of pure glycerin is 0.85 Pa s at 27 °C. The volume fraction of the particles Φ ranges here from 0.5% to 1.6%. Adding magnetic particles to glycerin varies its viscosity by a factor less than 2% [20].

3.1.2 Magnetic particles

Magnetic fluids are never monodisperse solutions of magnetic particles. The size distribution is assumed to be log-normal [21]. It is given by:

$$P(d) = \frac{1}{\sqrt{2\pi}sd} \exp\left(-\frac{\ln^2(d/d_0)}{2s^2}\right) \qquad (9)$$

Table 1. Characteristics of the ferrofluid samples (samples M_i are based on γ-Fe$_2$O$_3$, samples C_i are based on CoFe$_2$O$_4$) - Diameters d_0 and standard deviations s of $\ln(d)$ as determined from a magnetization measurement. Anisotropy parameters $\sigma = \frac{E_a}{kT}$ calculated using $E_a = K_s S$ with $S = \pi d_{mp}^2$ for γ-Fe$_2$O$_3$ samples and $E_a = K_V V$ with $V = \frac{\pi}{6} d_{mp}^3$ for CoFe$_2$O$_4$ samples; Measured values of the relaxation time $\tau_{exp} = \tau_{ani}$ in the range $H > H_a$ for γ-Fe$_2$O$_3$ samples; Brownian relaxation times τ_B deduced from an extrapolation at $H = 0$ of the experimental characteristic times τ_{exp}.

Glycerine, 27 °C	d_0 (nm)	s	σ	τ_{ani} (ms)	τ_B (ms)
M_1	9.4	0.1	1.8	0.46	0.81
M_2	9.2	0.15	1.7	0.75	1.27
C_1	12.7	0.35	35.9	–	4.45
C_2	9	0.2	16.4	–	1.44
C_3	8.7	0.16	15.4	–	0.38
C_4	7	0.2	7.7	–	0.44
C_5	6.6	0.5	3.4†	–	–

† This value is inaccurate because of the large polydispersity of the sample.

where $\ln(d_0)$ is the mean value of $\ln(d)$ and s is the standard deviation. The most probable diameter d_{mp}, which corresponds to the maximum of $P(d)$, is $d_{mp} = d_0 e^{-s^2}$. In a first approximation, each magnetic particle can be seen, as a magnetic monodomain. Its magnetic moment is $|\boldsymbol{\mu}| = m_S(\pi d_0^3/6)$, m_S being the saturation magnetization of the bulk magnetic material of the particle; for γ-Fe$_2$O$_3$ $m_S = 3.2 \times 10^5$ Am^{-1} and for CoFe$_2$O$_4$ $m_S = 3.5 \times 10^5$ Am^{-1} at room temperature. The size distribution of the particles can be deduced from an adjustment of the magnetization curve of the colloidal dispersion to a first Langevin law weighted by a log-normal distribution. The diameter d_0 and the standard deviation s of the present samples, deduced from such a procedure, are given in Table 1. Recent FMR measurements have demonstrated that our γ-Fe$_2$O$_3$ nanoparticles are magnetically uniaxial with an anisotropy of surface origin [22]: $E_a(\gamma$-Fe$_2$O$_3) = K_S S$ where $S = \pi d^2$ and $K_S = 2.8 \times 10^{-5}$ Jm^{-2}. The anisotropy field H_{ani} of γ-Fe$_2$O$_3$ nanoparticles (see Fig. 3) is related to the anisotropy constant K_S by $H_{ani} = (12/\mu_0 m_S)(K_S/d)$. It is typically of the order of 10^2 kA m^{-1} and $E_a(\gamma$-Fe$_2$O$_3)$ is here of the order of $k_B T$. γ-Fe$_2$O$_3$ nanoparticles behave as soft magnetic dipoles ($\sigma \approx 1$). On the contrary, the anisotropy field H_{ani} of CoFe$_2$O$_4$ nanoparticles, as deduced from the hysteresis loop of magnetization curves at a few Kelvin [23,24], is one order of magnitude larger (see Fig. 3). It does not seem to present any size dependence and is compatible with a volume anisotropy $E_a(CoFe_2O_4) = K_V V$ where $K_V = (1/2)\mu_0 m_S H_{ani} \approx 5 \times 10^5$ Jm^{-3}. This value of K_V is of the same order as what is found in [25] and [26]. The temperature dependence of the anisotropy of CoFe$_2$O$_4$ nanoparticles is here neglected. It is considered as a second order variation as it is in γ-Fe$_2$O$_3$ nanoparticles [22]. For CoFe$_2$O$_4$ nanoparticles, $E_a(CoFe_2O_4)$ is in the present experiment always larger than $k_B T$. CoFe$_2$O$_4$ nanoparticles should behave as rigid magnetic dipoles ($\sigma \gg 1$). Table 1
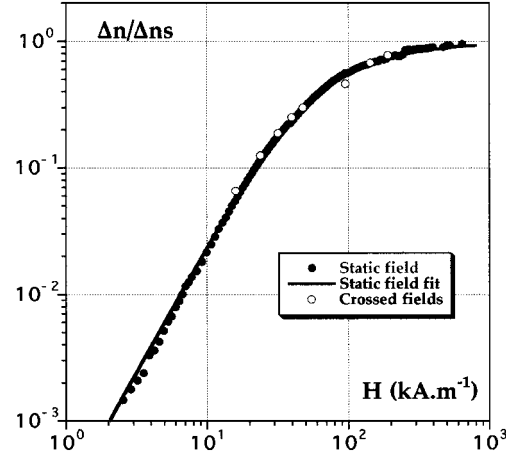
Fig. 4. Sample M_1. Comparison of static birefringence measurements (full symbols) to the experimental values obtained at 1 Hz with the crossed magnetic-fields device (open symbols). The full line corresponds to a best fit of equation (10) weighted by a log-normal distribution, as performed in reference [28].

gives $\sigma = E_a/k_B T$ for all the present samples. It is determined with $d = d_{mp}$, the most-probable diameter deduced from the magnetization measurements.

3.1.3 Magneto-optical properties

Our magnetic colloids, either based on γ-Fe$_2$O$_3$ nanoparticles or on CoFe$_2$O$_4$ nanoparticles, are optically isotropic in zero magnetic field. They become birefringent if a field is applied. The effect increases with the intensity of the applied field up to a saturation. If the colloid is correctly stabilized, as it is carefully checked here, the optical anisotropy of the solution comes from a progressive orientation of the magnetic particles along the field, the nanoparticles being themselves optically uniaxial [27–29].

Figure 4 presents a typical field-dependence of birefringence $\Delta n(H)$, that of sample M_1 (see Tab. 1), experimentally obtained here with a standard device [28] for measuring static birefringence. In a monodisperse approximation, the birefringence of the ferrofluid can be modelized as [28]:

$$\Delta n = \Phi \delta n_0 L_2(\xi) \qquad (10)$$

where δn_0 is the nanoparticle intrinsic birefringence with

– $\delta n_0 \approx$ const. for $\sigma \gg 1$,
– $\delta n_0 \propto \sigma$ for $\sigma \leq 1$,

and $L_2(\xi) = 1 - 3L_1(\xi)/\xi^2$ is the second Langevin function. The experimental curve $\Delta n(H)$ can be adjusted by equation (10) weighted by the log-normal size distribution (Eq. (9)). It leads to an optical size distribution determination. Figure 4 presents such a fit for sample M_1. The birefringence saturation gives a determination of δn_0. The particle size dependence of δn_0 has been experimentally investigated for CoFe$_2$O$_4$ particles in reference [27] and for γ-Fe$_2$O$_3$ particles in reference [28]. For
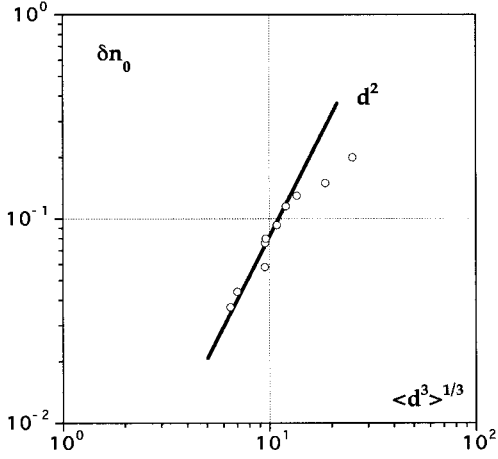
Fig. 5. δn_0 plotted as a function of $\langle d^3 \rangle^{1/3}$ (in nanometers). The experimental values come from reference [28]. The full line has a slope 2. Here the dependence on the polydispersity index is neglected (by opposition of what is done in Ref. [28]).
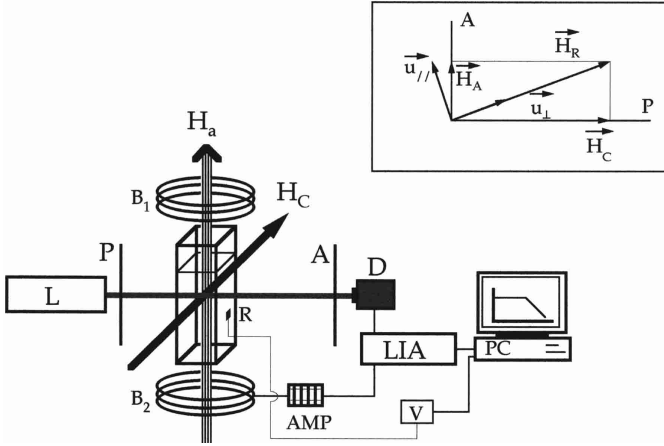
Fig. 6. Experimental set-up. The inset displays the orientation of the different optical devices.

CoFe$_2$O$_4$, δn_0 is found to be size independent and equal to $6.5 \times 10^{-2} \pm 0.6 \times 10^{-2}$. It optically states the rigid dipole behavior of those particles. On the contrary, for γ-Fe$_2$O$_3$, δn_0 is found to be size dependent. For the smallest diameters, it scales as d^2, the particle surface (see Fig. 5). This states optically the soft dipole behavior for γ-Fe$_2$O$_3$ particles. As in this case $\delta n_0 \propto \sigma \propto E_a$, it confirms by an optical measurement the surface scaling of $E_a(\gamma$-Fe$_2$O$_3)$ (for a particle diameter roughly less than 15 nm).

3.2 Experimental set-up in crossed fields

The experimental set-up with crossed magnetic fields is presented in Figure 6. A He-Ne laser beam of wavelength $\lambda_0 = 632.8$ nm and of weak power (1 mW) first goes through a polarizer (P). It then meets a non-birefringent silica glass cell of thickness e which contains the ferrofluid sample (S) to be probed. The cell thickness may vary from ten micrometers up to one millimeter depending on the

nanoparticle material and on the volume fraction of the sample. The thin optical cell is set between the polar pieces of an electromagnet producing the horizontal static magnetic field H_C of maximum amplitude 240 kA m^{-1}. Two coils (B$_1$,B$_2$) in Helmholtz's position generate a vertical and uniform magnetic alternating field H_A. Its amplitude ranges from 1.6 kA m^{-1} up to 5.6 k Am^{-1}. Under field, the sample cell behaves as an anisotropic plate and introduces a phase-lag between the two components of the wave electric field. The laser beam then passes through an analyzer. The transmitted light intensity is collected with a photodiode (PD) linked to a Lock-In Amplifier. This device is also generating an alternating tension which is amplified (AMP) to produce the alternating field H_A at half of the detection frequency. The temperature of the sample is continuously measured with a platinum probe (R) linked to a voltmeter (V) and maintained constant at $27 \pm 0.2\ °$C with a Peltier device.

3.3 Optical detection

The He-Ne laser beam is non-polarized. As the plane-wave electric field, propagating along the z direction, goes through the polarizer (see inset of Figure 3 for the respective directions of fields and optical devices), it gets a linear polarization and writes:

$$\mathbf{E}_P = E_{0P}\boldsymbol{\Pi}_P \quad \text{with} \quad E_{0P} = E_0 \cos(\omega_0 t - kz). \quad (11)$$

It then goes across the ferrofluid sample submitted to the resulting magnetic field $\mathbf{H}_R$. At the output of the cell sample, its polarization is now characterized by a phase-lag φ between its components. In complex notations, the real part φ' of the phase-lag writes $\varphi' = 2\pi e \Delta n / \lambda_0$ with Δn the birefringence of the sample of thickness e. The imaginary part φ'' of the phase-lag, which corresponds to the sample absorption, is defined by $\varphi'' = \ln \sqrt{t_\parallel / t_\perp}$; $t_\parallel$ (respectively $t_\perp$) being the transmission coefficient in the direction parallel (resp. perpendicular) to the resulting magnetic field. The electric field is then:

$$\mathbf{E}_P = E_{0P}\sqrt{t_\perp}[\exp(-\varphi'')\sin\theta\,\mathbf{u}_\parallel + \cos\theta \exp(\mathrm{i}\varphi')\mathbf{u}_\perp], \quad (12)$$

$\mathbf{u}_\parallel$ ($\mathbf{u}_\parallel \perp \mathbf{u}_\perp$) being the instant unit vector in the resulting magnetic field direction.

If $H_A = 0$, the static field is large and aligns on average the magnetic particles along its own direction. The optical axis of the sample is parallel to $\mathbf{H}_C$ [21]. The analyzer being perpendicular to $\mathbf{H}_C$, it is also perpendicular to the induced optical axis and the induced anisotropy cannot be detected.

If $H_A \neq 0$, this alternating magnetic field, normal to $\mathbf{H}_C$, produces a modulation of the direction of the optical axis. It is associated to a modulation of the birefringence. In our experimental configuration, we only detect this modulation of birefringence.

After the analyzer, the transmitted light is again linearly polarized and the wave electric field becomes:

$$\mathbf{E}_A = \frac{E_{0P}}{2}\sin(2\theta)\sqrt{t_\perp}[\exp(-\varphi'') - \exp(\mathrm{i}\varphi')]\boldsymbol{\Pi}_A \quad (13)$$

where $\theta = (\boldsymbol{\mu}, \mathbf{H}_C)$ (see Fig. 1). The light intensity measured by the photodiode after the analyser is given by:

$$I = |\mathbf{E}_A|^2 = E_{0P}^2 \sqrt{t_\parallel t_\perp} \sin^2(2\theta) \left(\sin^2 \left(\frac{\varphi'}{2} \right) + \text{sh}^2 \left(\frac{\varphi''}{2} \right) \right). \tag{14}$$

As the dichroism is weak compared to the birefringence of our ferrofluid samples [29], it comes $t_0 \approx t_\parallel \approx t_\perp$ and $\varphi = \varphi'$. If $2\theta \ll 1$, it gives the following detected light intensity:

$$I = |\mathbf{E}_A|^2 = 4t_0 E_{0P}^2 \theta^2 \sin^2 \left(\frac{\varphi'}{2} \right). \tag{15}$$

With our set-up I is proportional to θ^2 thus to $\tilde{\theta}^2 \exp(2i\omega t)$ (see Eq. (4)). It has only a 2ω component. We thus measure the amplitude and the phase of the signal at twice the excitation frequency. The collected light intensity is called $I_{2\omega}$ further on. If $\varphi'/2 \ll 1$, it writes:

$$I_{2\omega} = t_0 E_{0P}^2 \varphi'^2 \tilde{\theta}^2 \propto \Delta n^2 \tilde{\theta}^2. \tag{16}$$

3.4 Experimental conditions

The experiments are all performed at a ratio of the field amplitudes H_A/H_C such as $H_A/H_C \leq 0.1$.

The Brownian relaxation time τ_B of rotational diffusion of the nanoparticles in glycerin is about a millisecond. The condition $\omega\tau_B \approx 1$ then corresponds to a frequency $f_B \approx 200$ Hz. The experiment is performed for each couple of fields (H_A, H_C) scanning the frequency $f = \omega/2\pi$ from 1 Hz up to 1 kHz (or 10 kHz depending on the sample absorption). Measurements at 10 kHz are made only for the maghemite samples which are the less absorbing ones.

4 Results

In the experiments, the collected optical signal $I_{2\omega}$ is proportional to the square of the magnetically induced birefringence Δn in the sample. We collect both its amplitude A at 2ω and its phase-lag ψ with respect to the reference. All the ferrofluid samples of Table 1, based either on iron or cobalt ferrite particles, are probed here. The frequency dependence of A and ψ are directly related to that of $\tilde{\theta}^2$ (see Eq. (16)).

4.1 Limit of zero frequency

The lowest frequency of the experiment is $f_0 = 1$ Hz. It is here always much lower than the Brownian frequency $f_B = (2\pi\tau_B)^{-1}$ of the samples; then we assume $A(f_0) = \lim_{f\to 0} A(f)$ and $\psi(f_0) = \lim_{f\to 0} \psi(f)$. The validity of this assumption is demonstrated in Figure 4, for sample M_1 based on maghemite particles. Figure 4 plots the birefringence Δn obtained at f_0 with the crossed fields apparatus and compares it to the measurements obtained by a

static device. Note that at $f_0 = 1$ Hz, $\tilde{\theta} = \theta_0 = (\mathbf{H}_R, \mathbf{H}_C)$ then we get $\psi(f_0) = 0$ and $\Delta n(f_0) \propto \sqrt{A(f_0)}$, the proportionality factor being dependent on the laser intensity and on the sample absorption. We note further on A_0 for $A(f_0)$.

4.2 Argand diagrams

An Argand diagram is a plot of the modulus of the imaginary part $\text{Im}(I_{2\omega})$ of the signal as a function of its real part $\text{Re}(I_{2\omega})$. These two quantities are related to the amplitude A and the phase-lag ψ, here negative, by:

$$\text{Re}(I_{2\omega}) = A\cos\psi; \quad \text{Im}(I_{2\omega}) = A\sin\psi. \tag{17}$$

Figures 7a and b present Argand diagrams for the ferrofluid sample M_1 based on maghemite and the sample C_3 based on cobalt ferrite for different couples (H_A, H_C) of static and alternating fields with $H_A/H_C \leq 0.1$. In both figures, a master curve is obtained, independent on the particle material and independent on the values of H_A and H_C. This master curve can be compared to the theoretical model of part 2.

The experimental signal $I_{2\omega}$ is proportional to $\tilde{\theta}^2$ thus to $(1+i\omega\tau)^{-2}$ in the framework of the Debye model of the part 2 (see Eq. (4)). We obtain for the amplitude A and the phase-lag ψ:

$$\begin{cases} A/A_0 = 1/(1 + \omega^2\tau^2) \\ \psi = \text{Arctan}(-2\omega\tau/(1 - \omega^2\tau^2)) \end{cases} \tag{18}$$

and for the real and imaginary parts:

$$\begin{cases} \text{Re}(I_{2\omega}/A_0) = \dfrac{1 - \omega^2\tau^2}{(1 + \omega^2\tau^2)^2} \\ \text{Im}(I_{2\omega}/A_0) = \dfrac{-2\omega\tau}{(1 + \omega^2\tau^2)^2}. \end{cases} \tag{19}$$

In expressions (18) and (19) $\omega\tau$ appears as a reduced parameter. The Argand representation leads to a cardioid curve where $\omega\tau$ is a silent parameter. Figures 7a and b compares the plot of equation (19) together with the experimental data. The fit is quite good. To go further on in the interpretation of the results, it is necessary to determine τ for each sample as a function of the applied field.
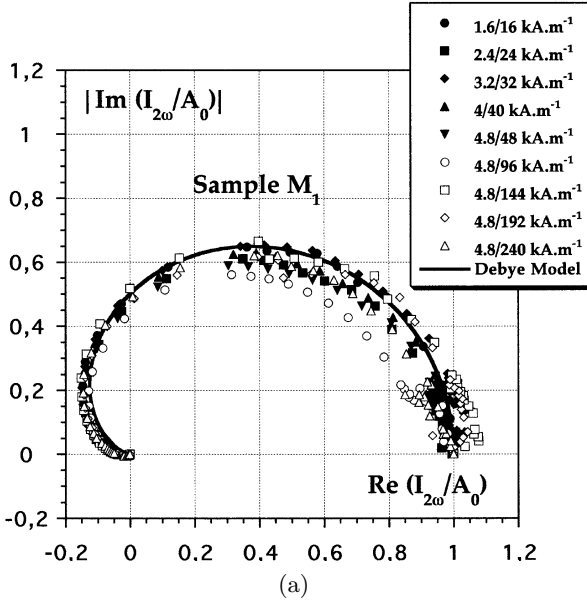
For $\omega\tau = 1$, we obtain from equation (18), (19):

$$\begin{cases} A/A_0 = 1/2 \\ \psi = -90° \end{cases} \text{and} \begin{cases} \text{Re}(I_{2\omega}/A_0) = 0 \\ \text{Im}(I_{2\omega}/A_0) = -1/2. \end{cases} \tag{20}$$
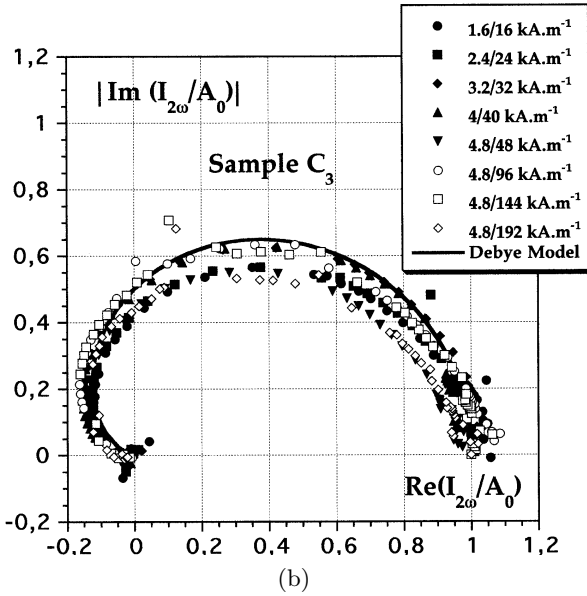
For a τ determination a direct plot of those quantities is much more convenient than an Argand representation.

4.3 Determination of a characteristic time

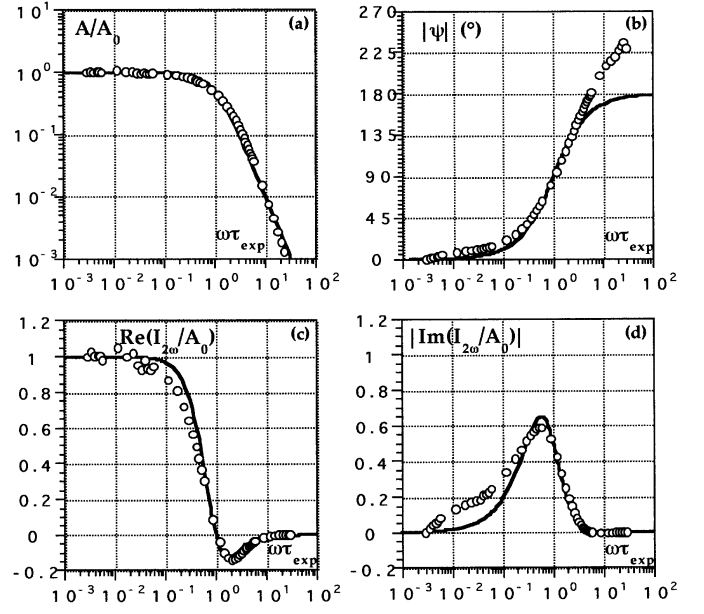For the experimental determination of the characteristic relaxation time τ we choose the criterion

Fig. 7. Argand diagram for ferrofluid samples (a): sample M_1 based on γ-Fe$_2$O$_3$ nanoparticles. (b): sample C_3 based on CoFe$_2$O$_4$ nanoparticles.

Fig. 8. Sample M_1 based on γ-Fe$_2$O$_3$ nanoparticles at $H_C = 48$ kAm^{-1} and $H_A = 4.8$ kAm^{-1} ($\tau_{\exp} = 0.46$ ms). (a) Amplitude, (b) modulus of the phase-lag; (c) real part; (d) modulus of the imaginary part of the signal as a function of the reduced parameter $\omega\tau_{\exp}$. The solid curves correspond to the theoretical expressions (18) and (19) obtained in the framework of a Debye model.
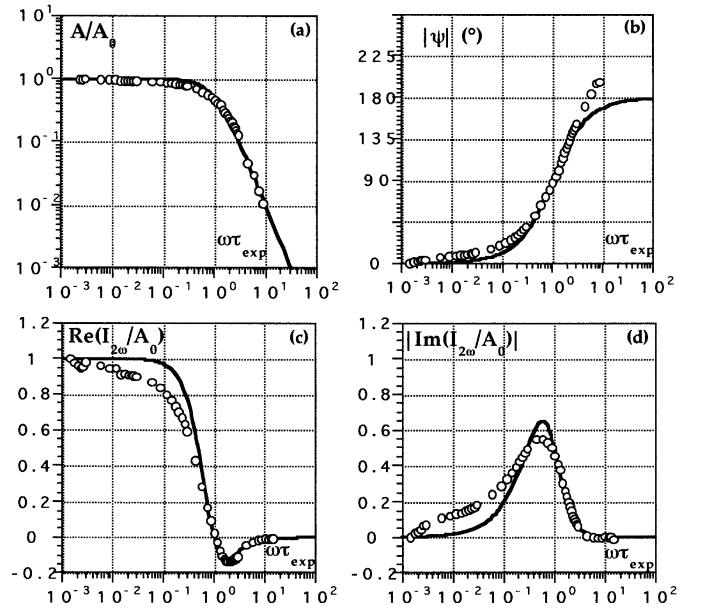
Fig. 9. Sample C_3 based on CoFe$_2$O$_4$ nanoparticles at $H_C = 48$ kAm^{-1} and $H_A = 4.8$ kAm^{-1} ($\tau_{\exp} = 0.23$ ms). (a) Amplitude, (b) modulus of the phase-lag; (c) real part; (d) modulus of the imaginary part of the signal as a function of the reduced parameter $\omega\tau_{\exp}$. The solid curves correspond to the theoretical expressions (18) and (19) obtained in the framework of a Debye model.

$A(\omega\tau = 1)/A_0 = 0.5$. It is determined for each ferrofluid sample and for each couple (H_C, H_A). We note this relaxation time $\tau_{\exp}$. As an example, we find $\tau_{\exp} = 0.46$ ms for sample M_1 and $\tau_{\exp} = 0.23$ ms for sample C_3. Figures 8 and 9 are an illustration of the quality of this $\tau_{\exp}$ determination. They present the four theoretical expressions of equations (18) and (19) as a function of the reduced parameter $\omega\tau = \omega\tau_{\exp}$. These theoretical predictions are plotted together with the experimental data ($\tau_{\exp}$ being already determined) at $H_C = 48$ kA m^{-1} and $H_A = 4.8$ kA m^{-1} for the two samples M_1 (γ-Fe$_2$O$_3$) and C_3 (CoFe$_2$O$_4$). It is easy to check in Figures 8 and 9 that all the criterions of equation (20) are equivalent as well

for γ-Fe$_2$O$_3$ particles and CoFe$_2$O$_4$ ones. The main discrepancy between the data and the theoretical description concerns the phase-lag ψ at the highest frequencies in the experimental range where the signal is the weakest. The amplitude at the highest frequencies is of the order of 1% to 1 of the amplitude at 1 Hz and becomes close to the limit of detection (1 μV). The phase-lag determination is then very poor. However, it does not penalize the $\tau_{\exp}$ determination.

4.4 Various experimental regimes of characteristic times

We present below the experimental dependence of the measured characteristic times. We compare them with the theoretical predictions of Section 2. In our experiment we probe two different kinds of samples, with anisotropy fields differing by one order of magnitude at least. We thus expect for the two kinds of particles, two different dynamic regimes.
– For the CoFe$_2$O$_4$ particles, we have always $H_{\mathrm{R}} \ll H_{\mathrm{ani}}$ and the particles should behave as rigid dipoles.
– For the γ-Fe$_2$O$_3$ particles on the contrary, we have $\sigma \approx 1$ and a soft dipole behavior is expected. The condition $H_{\mathrm{R}} \geq H_{\mathrm{ani}}$ can be experimentally fulfilled.

4.4.1 Rigid dipoles ($\sigma \gg 1$)

For CoFe$_2$O$_4$ particles, the whole range of experimental magnetic fields H_{R} ($\approx H_{\mathrm{C}}$) corresponds to $H_{\mathrm{C}} \ll H_{\mathrm{ani}}$ (see Fig. 3). Figure 10a shows the experimental variations of the characteristic time $\tau_{\exp}$ as a function of the applied static magnetic field H_{C} for two samples (C$_1$ and C$_3$). As expected in Figure 2, the characteristic time is a decreasing function of the applied field. The experimental data can be fitted (solid lines of Fig. 10a) by the theoretical expression given in Section 1.1 (Eq. (6)); τ_{B}, the characteristic time in zero field being a free parameter. The τ_{B} values obtained with the fit are given in the Table 1. These values largely depend on the particle size distribution.

Figure 10b is a log-log plot of the characteristic time $\tau_{\exp}$ as a function of the static magnetic field H_{C} for the different cobalt ferrite samples in the restricted experimental range $\tau_{\exp} \leq \tau_{\mathrm{B}}/2$. In that domain $\tau_{\exp}$ should roughly reach its asymptotic value τ_{H} (see Eq. (5) and Fig. 2). The master curve of Figure 10b clearly shows that with our samples based on cobalt ferrite particles the rigid dipole regime for which $\tau_{\exp} = \tau_{\mathrm{H}} \propto H_{\mathrm{C}}^{-1}$ is observed in our experiment. In that high field regime the characteristic time is at the first order independent of the particle size distribution.

4.4.2 Soft dipoles ($\sigma \approx 1$)

Figure 11a presents the measurements performed with the two ferrofluid samples based on maghemite particles for $H_{\mathrm{C}} \geq 90$ kA m^{-1}, approximate value of their anisotropy
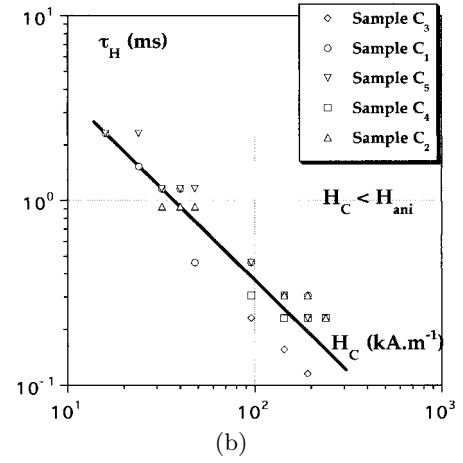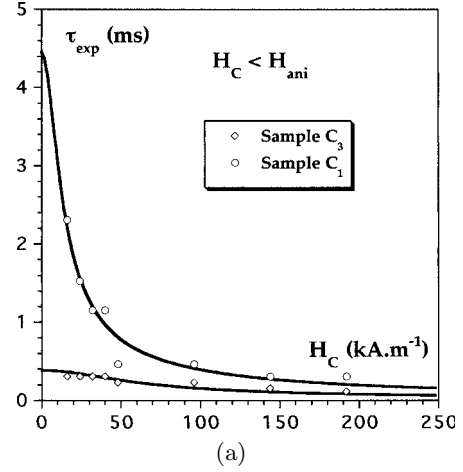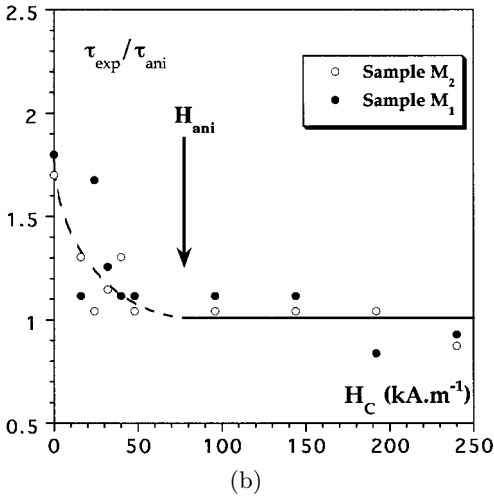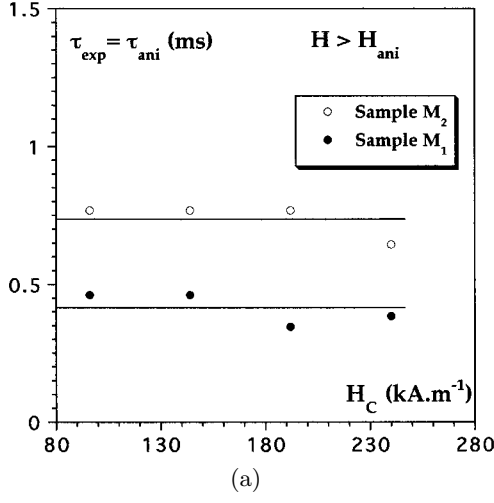

Fig. 10. Cobalt ferrite samples. Here $H_{\mathrm{C}} \ll H_{\mathrm{ani}}$. (a): Evolution of the characteristic relaxation time $\tau_{\exp}$ as a function of the static magnetic field H_{C} for samples C$_1$ and C$_3$. The full line corresponds to the fit $\tau_{\exp} = \tau_\perp$ from equation (6). τ_{B} is a free parameter given by the fit at $H_{\mathrm{C}} = 0$ (see Tab. 1). τ_{B} strongly depends on the particle size distribution. (b): log-log representation of $\tau_{\exp}$ as a function of the static magnetic field H_{C} in the asymptotic rigid dipole regime (the condition is here set at $\tau_{\exp} \leq \frac{\tau_{\mathrm{B}}}{2}$). The full line corresponds to $\tau_{\exp} = \tau_{\mathrm{H}} \propto H_{\mathrm{C}}^{-1}$. In this regime $\tau_{\exp}$ is independent of the particle size distribution of the sample.

field H_{ani}. In this regime, $\tau_{\exp}$ is a constant independent of H_{C} and $\tau_{\exp} = \tau_{\mathrm{ani}}$ (see Eq. (8)).

We find on average $\tau_{\mathrm{ani}} \approx 0.46$ ms for sample M$_1$ and $\tau_{\mathrm{ani}} \approx 0.75$ ms for sample M$_2$. This relaxation time is related to τ_{B} and σ through the relation $\tau_{\mathrm{ani}} = \tau_{\mathrm{B}}/\sigma$. As for each of the two samples we have an evaluation of σ, we may thus deduce a value of τ_{B} (see Tab. 1). As σ is roughly the same for the two samples, the experimental results $\tau_{\exp}/\tau_{\mathrm{ani}}$ scales on the same master curve (see Fig. 11b) on the whole range of magnetic fields here investigated. In Figure 11b, the value of $\tau_{\exp}/\tau_{\mathrm{ani}}$ in the limit $H = 0$ is $\tau_{\mathrm{B}}/\tau_{\mathrm{ani}} = \sigma$.
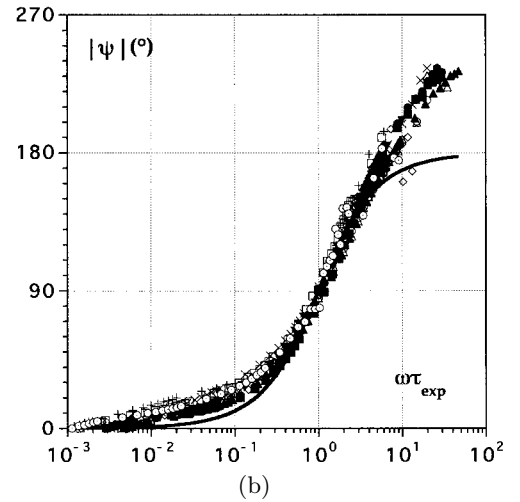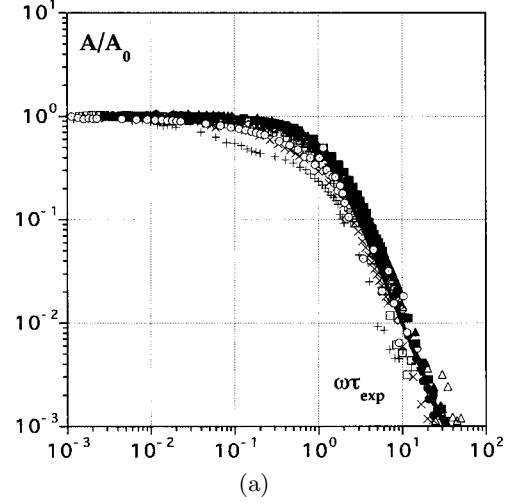
Fig. 11. Maghemite samples. (a): Evolution of the characteristic relaxation time $\tau_{\rm exp}$ as a function of the static magnetic field $H_{\rm C}$ for samples M_1 and M_2 in the soft dipole regime at $H_{\rm C} > H_{\rm ani}$. Full horizontal lines correspond to the asymptotic values $\tau_{\rm exp} = \tau_{\rm ani} =$ const. (see exp. (8)). (b): Reduced representation of $\tau_{\rm exp}/\tau_{\rm ani}$ as a function of $H_{\rm C}$ for the two samples M_1 and M_2. The full line corresponds to $\tau_{\rm exp} = \tau_{\rm ani} =$ const. The dashed line is a guide for the eye joining $(\tau_{\rm exp}/\tau_{\rm ani})_{H=0} = \sigma$ to the regime $\tau_{\rm exp}/\tau_{\rm ani} = 1$ observed for $H > H_{\rm ani}$.

Fig. 12. Master curves of amplitude (a) and modulus of the phase-lag (b) of $I_{2\omega}$ as a function of the reduced parameter $\omega\tau_{\rm exp}$ for various samples based on γ-Fe$_2$O$_3$ or CoFe$_2$O$_4$ nanoparticles at various couples of fields $H_{\rm C}$ and $H_{\rm A}$.

4.4.3 Issues

If for $\sigma \gg 1$ and $\sigma \approx 1$, the low field behaviors of $\tau_{\rm exp}$ are very similar, its high field behaviors are clearly different for rigid and soft dipoles. This point appears to be true both theoretically and experimentally. For $H_{\rm C} > H_{\rm ani}$, $\tau_{\rm exp}$ is a constant while for $H_{\rm C} < H_{\rm ani}$ it varies as $H_{\rm C}^{-1}$. A measurement of $\tau_{\rm exp}$ as a function of $H_{\rm C}$ can distinguish easily a rigid dipole from a soft one. The determination of the cross-over field above which $\tau_{\rm exp}$ becomes a constant, can be seen as a measurement of the anisotropy field. Such

an $H_{\rm ani}$ determination could reveal itself useful for soft dipoles in the near future.

4.5 General master curves

Using the experimental determinations of $\tau_{\rm exp}$, for both soft and rigid dipole regimes, all the experiments under field may be grouped on general master curves. In Figures 12a and b, amplitude and phase are plotted as a function of the reduced parameter $\omega\tau_{\rm exp}$. Whatever the nature of the nanoparticle material and whatever the applied field $H_{\rm R}$, all the experiments reduce to a general behavior well described by the theoretical expressions (Eq. (18)). The polydispersity of the samples may explain the slight deviation of the phase behavior with respect to the theoretical

model for $\omega\tau_{\mathrm{exp}} < 1$. At high frequencies ($\omega\tau_{\mathrm{exp}} > 3$), this discrepancy becomes large. It should be noted that in this experimental range the intensity of the signal $I_{2\omega}$ is very low and close to the detection limit ($1\ \mu$V). It heavily penalizes the accuracy of the measurement of the phase-lag Ψ for the highest fields.

Whatever the kind of particles used here, being rigid dipoles or soft ones, the same master curves are obtained in the representations of Figure 12. They are basically characteristic of the viscous response of the nanoparticle carrier (see exp. (3)). Here this carrier is a Newtonian liquid. Indeed in a visco-elastic carrier or a liquid-crystalline matrix we expect strong distortions with respect to representations such as these of Figure 12.

5 Discussion

Our simple mechanical model describes quite reasonably our whole experimental results whatever the particle material, the particle size and the applied magnetic field. The polydispersity of the particle size distribution is not taken in account here. An improvement of the model could be imagined introducing a relaxation of the form $I_{2\omega} \propto [1/1 + (\mathrm{i}\omega\tau)^{\alpha}]^2$, α being a Cole-Cole exponent related to the sample polydispersity [30]. However such a refinement does not seem relevant here as the main criticism to address to the present theoretical description is that it is a "vectorial" approach which assimilates the dynamics of $\boldsymbol{\mu}$ to that of the birefringence. Birefringence is basically a tensorial quantity [31], a further better model should first take this point into account. Nevertheless, the present approach is an interesting first step to describe the dynamical birefringence of magnetic fluids.

The dynamic of the magnetic moment can be directly probed experimentally. Measuring the low-field complex susceptibility [12] or the relaxation of magnetization [13] can do it. The Brownian relaxation investigated in the present work can be also evidenced by these methods. However Néel relaxation can never be forgotten and always contribute experimentally for a part of the magnetic signal. The decisive advantage of magneto-optical dynamical birefringence is that it only probes the mechanical rotation of the grains, being not directly sensitive to the Néel process. The behaviors found here are characteristic of a liquid carrier, it distinguishes several magnetic regimes for the relaxation time. The field dependence of the relaxation time is quite different for $\sigma \gg 1$ and for $\sigma \approx 1$. This property will be used in future to evaluate the anisotropy field of other nanoparticle materials, such as $\mathrm{NiFe_2O_4}$, $\mathrm{ZnFe_2O_4}$ or $\mathrm{CuFe_2O_4}$, recently synthesized [32] and not yet fully characterized.

This work will be also important as a reference basis to understand a future probing of more complicated carrier media. If magnetic particles are dispersed in a complex medium such as a solution of long polymeric chains, the Argand plots of Figure 7 may become two bump curves [33]. It reveals then a complicated dynamics: – that of free rotating particles, – that of particles whose rotation is hindered by the long chains. Those particles coexist with a third population, almost blocked particles that can only contribute to the birefringence signal through a slow non-ergodic relaxation. By reference to the master curves of the present paper, it will be possible to clearly distinguish a standard viscous behavior from a visco-elastic one, which could also present a resonance, or from a glassy one. However another decisive advantage of the present method is to be able to investigate the local rheology of liquid-crystalline matrices doped with magnetic nanoparticles [3,4,8,9]. The device developed here investigates the mechanical response of the particles in the plane defined by the two crossed magnetic fields. The crossed-field experiment will be particularly powerful to probe the dynamics of anisotropic media doped with ferrofluid particles.

6 Conclusion

The magneto-optical birefringence response of magnetic fluids to a static magnetic field H_{C} crossed with a smaller alternating one is probed here. The in-phase and the out of phase components are compared with a very simple model which reproduces the main frequency dependence. A reduced parameter $\omega\tau_{\mathrm{exp}}$ allows to re-scale all the experimental results together. In the present study we evidence several magnetic regimes for the particles:
– using cobalt ferrite nanoparticles we explore the rigid dipole regime ($\sigma \gg 1$) in the range $H_{\mathrm{C}} \ll H_{\mathrm{ani}}$ where $\tau_{\mathrm{exp}} = \tau_{\mathrm{H}} \propto H_{\mathrm{C}}^{-1}$,
– using maghemite nanoparticles, we explore the soft dipole regime ($\sigma \approx 1$) in the range $H_{\mathrm{C}} > H_{\mathrm{ani}}$ where $\tau_{\mathrm{exp}} = \tau_{\mathrm{ani}} \approx \mathrm{const}$.

In future, an experimental probing of more complex magnetic media will require to improve the rough mechanical description developed here in a theoretical model taking into account the tensorial nature of optical birefringence.

References

1. R.E. Rosensweig, *Ferrohydrodynamics* (Cambridge University Press, New-York 1985).
2. J.C. Bacri, D. Gorse, J. Phys. France **44**, 985 (1983).
3. P. Fabre, C. Cassagrande, M. Veyssie, V. Cabuil, R. Massart, Phys. Rev. Lett. **64**, 539 (1990).
4. V. Berejnov, J.C. Bacri, V. Cabuil, R. Perzynski, Yu.L. Raikher, Europhys. Lett. **41**, 507 (1998).
5. J.C. Bacri, J. Dumas, D. Gorse, R. Perzynski, D. Salin, J. Phys. Lett. France **46**, L-1199 (1985).

6. J.C. Bacri, K. Djerfi, S. Neveu, R. Perzynski, J. Magn. Magn. Mater. **123**, 67 (1993).
7. A. Halbreich, J. Roger, J.-N. Pons, M. Fatima Da Silva, E. Hasmonay, M. Roudier, M. Boynard, C. Sestier, A. Amri, D. Geldweth, B. Fertil, J.-C. Bacri, D. Sabolovic', in *Scientific and Clinical Applications of Magnetic Carriers*, edited by W. Schutt, J. Teller, U. Häfeli, M. Zborowski (Plenum Press, New-York, 1997) p. 399.
8. J.C. Bacri, A.M. Figueiredo Neto, Phys. Rev. E **50**, 3860 (1994).
9. D. Spolianski, J. Ferre, J.P. Jamet, V. Ponsinet, J. Magn. Magn. Mater. **201**, 200 (1999).
10. M.J. Shliomis, Sov. Phys. Usp. **17**, 153 (1974).
11. L. Neel, C. R. Acad. Sc. Paris **228**, 664 (1949); Ann. Geophys. **5**, 99 (1949).
12. P.C. Fannin, S.W. Charles, J. Phys. D Appl. Physics **22**, 187 (1989).
13. R. Kötitz, P.C. Fannin, L. Trahms, J. Magn. Magn. Mater. **149**, 42 (1999).
14. M.A. Martsenyuk, Yu.L. Raikher, M.I. Shliomis, Sov. Phys. JETP **38**, 413 (1974).
15. E. Blums, A. Cebers, M.M. Maiorov, *Magnetic Fluids* (Walter de Gruyter, Berlin, 1997).
16. R. Massart *et al.*, Fr. Patent 2662539 (29-11-91), De. Patent 4116093 (28-11-91).
17. E. Dubois, Ph.D. thesis, University Pierre et Marie Curie, Paris, France 1997.
18. R. Massart, E. Dubois, V. C, E. Hasmonay, J. Magn. Magn. Mater. **149**, 1 (1995).
19. F.A. Tourinho, R. Franck, R. Massart, J. Mat. Sci. **25**, 3249 (1990).
20. E. Hasmonay, Ph.D. thesis, University Pierre et Marie Curie, Paris, France 1998.
21. *Magnetic Fluids and Applications Handbook*, edited by B. Berkovski (Begell House Inc. Publ., New-York, 1996).
22. F. Gazeau, J.-C. Bacri, F. Gendron, R. Perzynski, Yu.L. Raikher, V.I. Stepanov, E. Dubois, J. Magn. Magn. Mater. **186**, 175 (1998).
23. J. Tejada, LL. Balcells, S. Linderoth, R. Perzynski, B. Rigau, B. Barbara, J.-C. Bacri, J. Appl. Phys. **73**, 6952 (1993).
24. F. Gazeau, Ph.D. thesis, University Pierre et Marie Curie, Paris, France 1997.
25. S.W. Charles, S. Wells, Magnitnaya Gidrodinamika **26**, 30 (1990).
26. K.J. Davies, S. Wells, R.V. Upadhyay, S.W. Charles, K. O'Grady, M. ElHilo, T. Meaz, S. Morup, J. Magn. Magn. Mater. **149**, 14 (1995).
27. S. Neveu-Prin, F.A. Tourinho, J.-C. Bacri, R. Perzynski, Colloids Surf. A **80**, 1 (1993).
28. E. Hasmonay, E. Dubois, J.-C. Bacri, R. Perzynski, Yu.L. Raikher, V.I. Stepanov, Eur. Phys. J. B **5**, 859 (1998).
29. F. Bentivegna, M. Nyvlt, J. Ferre, J.P. Jamet, A. Brun, S. Visnovsky, R. Urban, J. Appl. Phys. **85**, 2270 (1999).
30. B. Castaing, J. Souletie, J. Phys. I France **1**, 403 (1991).
31. YU.L. Raikher, V.I. Stepanov, Europhys. Lett. **32**, 589 (1995).
32. M.H. Sousa, F.A. Tourinho, J. Depeyrot, G.J. Da Silva, M.C. Lara, J. Phys. Chem. B **105**, 1168 (2001).
33. J. Bacri, R. Perzynski, Lect. Notes Phys., edited by L. Garrido (Springer Verlag); Complex Fluids **415**, 100 (1993).